

THE NATURE OF THE DENSE CORE POPULATION IN THE PIPE NEBULA: CORE AND CLOUD KINEMATICS FROM C¹⁸O OBSERVATIONS

AUGUST A. MUENCH¹, CHARLES J. LADA¹, JILL M. RATHBORNE¹,
 JOÃO F. ALVES², & M. LOMBARDI^{3,4}

VERSION February 5, 2008; Submitted June 11, 2007

ABSTRACT

We present molecular-line observations of 94 dark cloud cores identified in the Pipe nebula through near-IR extinction mapping. Using the Arizona Radio Observatory 12m telescope, we obtained spectra of these cores in the J=1-0 transition of C¹⁸O. We used the measured core parameters, T_R^* , Δv , v_{lsr} , radius and mass, to explore the internal kinematics of the cores as well as their radial motions through the larger molecular cloud. We find that the vast majority of the dark extinction cores are true cloud cores rather than the superposition of unrelated filaments. While we identify no significant correlations between the core's internal gas motions and the cores' other physical parameters, we identify spatially correlated radial velocity variations that outline two main kinematic components of the cloud. The largest is a 15 pc long filament that is surprisingly narrow both in spatial dimensions and in radial velocity. Beginning in the Stem of the Pipe, this filament displays uniformly small C¹⁸O linewidths ($\Delta v \sim 0.4 \text{ km s}^{-1}$) as well as core to core motions only slightly in excess of the gas sound speed. The second component outlines what appears to be part of a large (2pc; $10^3 M_\odot$) ring-like structure. Cores associated with this component display both larger linewidths and core to core motions than in the main cloud. The Pipe Molecular Ring may represent a primordial structure related to the formation of this cloud.

Subject headings: Dust, extinction — ISM: individual (Pipe Nebula) — ISM: clouds — ISM: kinematics and dynamic — radio lines: ISM — stars: formation

1. INTRODUCTION

The Pipe nebula is a nearby (130 pc), large (15 pc) dark molecular cloud lying in projection against the Galactic bulge ($l \sim 0^\circ$; $b \sim 5^\circ$) and visible to the unaided eye. In addition to being one of the most nearby dark clouds it is unique for its apparent lack of star formation. Comparing large scale CO maps to IRAS point sources, Onishi et al. (1999) found only a single site of star formation (Barnard 59; Reipurth et al. 1996; Brooke et al. 2007) although their observations also revealed numerous dense (C¹⁸O) cores of gas. Given this lack of star formation, the Pipe nebula represents a good target for improving our understanding of the formation and early evolution of dark clouds before the star formation process has confused or significantly modified a cloud's internal structure or kinematics. Indeed, the Pipe cloud probably lies at the threshold before star formation begins and its internal structure and kinematics represent the initial conditions of star formation needed to guide theoretical models.

The physical structure of a dark cloud is best revealed through measurements of the dust; in particular through the mapping of the extinguishing of the starlight of background stars by this dust (Wolf 1923; Lada et al. 1994; Cambrésy 1999; Alves et al. 2001; Dobashi et al. 2005).

¹ Smithsonian Astrophysical Observatory. 60 Garden Street, Mail Stop 72, Cambridge, MA 02138 USA;
 gmuench@cfa.harvard.edu

² Calar Alto Observatory. Centro Astronómico Hispano Alemán, c/Jesús Durbán Remón 2-2, 04004 Almería, Spain

³ European Southern Observatory. Karl-Schwarzschild-Str. 2, 85748 Garching, Germany

⁴ University of Milan, Department of Physics. via Celoria 16, 20133 Milan, Italy

Lombardi et al. (2006) used a multi-band near-IR technique (NICER; Lombardi & Alves 2001) to create a detailed extinction map of the Pipe nebula at a resolution of $\sim 1'$. Filamentary structures with column densities as low as $A_V \sim 1$ mag can be seen weaving through the Pipe and this extinction map has a spatial resolution and a density contrast ideal for investigating primordial cloud structure. Alves et al. (2007) combined a wavelet analysis of the cloud with a clump finding routine to identify 159 significant column density enhancements that we will term dark extinction "cores." This terminology follows the literature usage of identifying dark regions of optical extinction (e.g. Lee & Myers 1999) or dust continuum peaks (e.g. Motte et al. 1998) as the cores of molecular clouds. We note that there is no consensus on the defining characteristics of a cloud core; some researchers in the field suggest that the terminology of a "core" should be applied only to those objects that are gravitationally bound. For this work we retain the use of the term "core," while also noting that such a determination cannot be made from dust absorption measurements alone.

Molecular-line observations are important to confirm that extinction cores are dense coherent kinematic structures and not the random superposition of cloud features such as filaments or multiple cloud cores. Molecular-line observations trace both "microscopic" internal motions such as turbulence, infall, rotation and expansion and any "macroscopic" bulk mass motions of the dark cores through the large ($10^4 M_\odot$) cloud. Thus, gas tracers are very useful for extracting the kinematics of dark clouds. Here we use molecular gas tracers to explore the kinematic state of the Pipe extinction cores identified in Alves et al. (2007). Specifically, we use observations of C¹⁸O at 3mm to measure the extinction cores' non-thermal inter-

TABLE 1
OBSERVING LOG

Date-Obs	2005			2006		
	T_{sys}	N_{obs}	Date-Obs	T_{sys}	N_{obs}	
2005-05-10	270-370	19	2006-01-28	240-280	8	
2005-05-11	280-360	23	2006-01-29	310-430	9	
2005-05-12	240-330	36	2006-01-30	240-440	10	
2005-05-19	340-490	18	2006-01-31	210-290	7	
2005-06-25	490-700	11	2006-02-01	230-270	9	
			2006-02-02	240-290	10	

nal motions as well as their ballistic motion through the ambient cloud traced by their radial velocity. This paper is the first in a series exploring the nature of the Pipe extinction cores by integrating tracers of molecular gas at a range of densities with the structure provided by the extinction map. In Rathborne et al. (2007) we use ammonia observations to explore the densest gas in the cores, deriving kinetic gas temperatures and probing the cores' chemical state. Finally, Lada et al. (2007) provides a synthesis of these results and examines their implications for the ability of these extinction cores to form young stars and, thus, provide an origin for the stellar initial mass function. This paper is organized simply into three subsequent sections. First, we detail our collection of C¹⁸O data for 94 of the 159 Pipe extinction cores identified by Alves et al. (§2), finding the vast majority to be coherent cloud structures. In §3 we analyze the completeness and homogeneity of our dataset, and we explore correlations between the extinction cores' structure and internal gas kinematics. Finally, we use our data to examine the large scale motions of the cores through the Pipe cloud (§4), revealing large (10 pc) coherent structures, including a large Ring similar to those found in the Taurus star forming region.

2. DATA

2.1. Telescope

Our goal was to survey the molecular gas properties of dark extinction cores identified by Alves et al. (2007) in the 2MASS NICER map of Lombardi et al. (2006). To complete this goal we used the Arizona Radio Observatory Kitt Peak 12m telescope (hereafter the ARO12m) for 12 nights over a 2 year period (2005-2006). We observed single center pointings of the J=1-0 line of C¹⁸O for each core. Table 1 lists the dates of our observations as well as the typical system temperatures (T_{sys}) and the number of pointings achieved per night; from Tucson, Arizona the Pipe nebula has a maximum visibility (el > 10°) window less than 5 hrs. All observations were performed remotely from Cambridge, Massachusetts, USA.

2.2. Technique

We next summarize the observational technique used to obtain the C¹⁸O data with the ARO12m. Observations were performed using the 3mm receiver (90-116 GHz) operating in frequency switching mode with the millimeter auto correlator. The correlator was configured in dual-polarization mode with 75 MHz usable bandwidth in each of 2 IF banks, having 16384 channels and an effective spectral resolution of 24.4 KHz/channel or

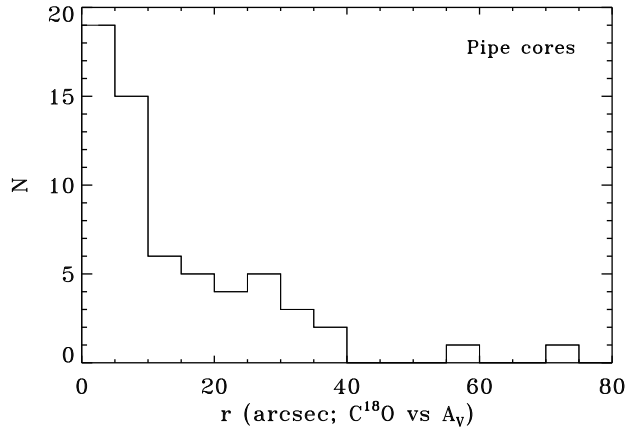


FIG. 1.— Positional offsets (r_{sep}) between the ARO12m C¹⁸O 56'' beam and the extinction core position reported in Alves et al. (2007). Note, the ARO12m C¹⁸O beam was centered on the extinction peak of each core.

0.067 km s⁻¹ at 109 GHz. We frequency switched at 5 Hz with a 2 MHz throw; the cloud appears projected against the Galactic bulge and we did not expect nor did we observe any molecular gas not associated with nearby gas clouds (v_{lsr} between 0-20 km s⁻¹). Spectral observations at the ARO12m use chopper-wheel calibration to correct for atmospheric attenuation and telescope losses. This places our data on the T_R^* temperature scale (Kutner & Ulich 1981). The source main beam brightness temperature, T_{mb} , is related to T_R^* by T_R^*/η_m^* , where $\eta_m^* = 0.97$ at 109GHz at the ARO12m, assuming that the source fills the main beam.

The standard observation had an integration time of 10 minutes. For each target, we repeated the standard observation until we achieved a root mean square noise of < 0.1 K per channel; total integrations ranged from 10 to 60 minutes and this value depended more on the target's elevation than its C¹⁸O brightness. All Pipe extinction cores in our sample were detected (at 3σ or greater) in C¹⁸O with the weakest line having $T_R^* = 0.14K$ (Pipe-100). Individual spectra were summed, folded, baseline subtracted and Gaussian profile fit using CLASS. The reduced results assume a rest frame frequency for C¹⁸O J=1-0 of 109782.173 MHz; this value was determined empirically by Lee et al. (1999, 2001).

2.3. Targets

In this section we describe the targets selected for these observations. The 56'' beam of the ARO12m at 109 GHz is well matched to the Gaussian kernel used by Lombardi et al. (2006) to filter spatially individual star extinction estimates derived from the 2MASS point source catalog. The final 2MASS extinction map has a resolution of 60'' FWHM Gaussian and was Nyquist sampled to a pixel scale of 30''. Additionally, the ARO12m beam is much smaller than the 2.7' beam used by Onishi et al. (1999) to create under-sampled C¹⁸O maps of ¹³CO cores (differences in beam size and resolution are discussed in §3.3.1). Given this optimized beam we targeted localized peaks of interstellar extinction throughout the Pipe nebula and assigned priority based initially on maximum column density. We revised our target priorities after the first year's observations to sample lower mass dark cores. In summary we obtained single pointing C¹⁸O data for

TABLE 2
C¹⁸O DATA

Pipe (ID)	flag (a)	Position (J2000)		r_{sep} ('')	v_{lsr} (km s $^{-1}$)	dv	T_R^* (K)	rms	$\Sigma A_V^{(b)}$ (mag.)
6		17:10:31.01	-27:25:33.31	8.07	3.501	0.391	2.066	0.06	99.6
7		17:11:36.39	-27:33:50.70	19.97	3.935	0.517	1.366	0.05	85.6
8		17:12:15.04	-27:37:44.41	2.76	3.462	0.390	2.012	0.05	88.7
11		17:10:49.87	-27:23:04.07	6.06	3.446	0.455	1.524	0.07	85.2
13		17:10:47.22	-27:13:41.43	9.64	3.751	0.336	0.498	0.05	39.4

NOTE. — Full version given at end of document (Table 7).

(a) Flag given to indicate C¹⁸O component for each extinction core. Components “a”, “b”, etc are ordered by antenna temperature. Where given, a Flag=2, corresponds to all components fit with a single Gaussian. (b) Total column density expressed in magnitudes of extinction (A_V) measured in a Gaussian weighted 56'' beam on the NICER 2MASS map of Lombardi et al. (2006) and centered on the position of the C¹⁸O observation.

94 of the 159 Pipe extinction cores; these targets span the entire range of core mass (0.2 to 20 M_\odot ; Alves et al. 2007). The completeness and homogeneity of this sample of cores are examined in §3.

While we targeted the localized extinction peak within each Pipe core, our pointing centers correspond very closely to the core centers reported in Alves et al. (2007)⁵, lying typically within a single resolution element of the A_V map. The distribution function of separations between the published core centers and the C¹⁸O pointings is given in Figure 1.

2.4. Results

We provide C¹⁸O observations for 94 Pipe extinction cores in Table 2. Identifications correspond to the core ID given by Alves et al. (2007)⁶ and are identical to those given in Lada et al. (2007). The Table includes the pointing center for each C¹⁸O observation and the results of a Gaussian profile fit.

Nine extinction cores (10% of the sample) displayed multi-peaked profiles in C¹⁸O; four of these cores consist of two and in one case three distinct lines. We record in the Table individual Gaussian fits to each component, identifying the stronger(T_R^*) line as the “a” cloud. In four of the nine cases the lines are sufficiently blended that in addition to multicomponent fits we also tabulated the fit of a single Gaussian to the double-peaked profile. We further analyze kinematically distinct and overlapping cloud components in §4.1.

3. ANALYSIS

3.1. Completeness

In this section we examine the completeness as a function of extinction core mass for our sample of 94 cores for which we obtained C¹⁸O line measurements. In Figure 2 we compare the mass function of all 159 Pipe cores to the mass function for our sample with C¹⁸O data. Note that the masses (M_{core}) and radii of the extinction cores used in this paper were derived by and are found in Lada et al. (2007). Briefly, Lada et al integrated the background subtracted extinction map of Alves et al. (2007)

⁵ The centers for the Pipe extinction cores listed in Alves et al. were derived using a 2D version of Clumpfind (Williams et al. 1994).

⁶ The Alves et al. extinction core identifications and positions can be obtained using the VizieR service <http://vizier.cfa.harvard.edu/> and have the catalog id of J/A+A/462/L17.

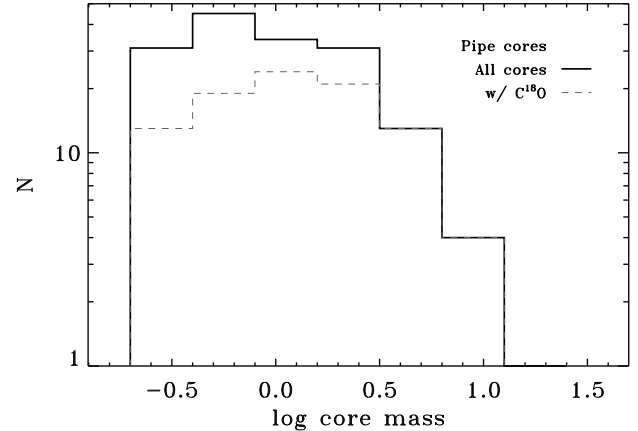


FIG. 2.— Completeness of CO sample. Mass functions for all 159 extinction cores (solid line) and for extinction cores with C¹⁸O measurements (dashed line) are compared. Masses are taken from the wavelet subtracted map as tabulated in Lada et al. (2007).

TABLE 3
C¹⁸O CORE COMPLETENESS

$\log M_\odot$	Full catalog			Stem and Bowl		
	N_{cores}	N_{obs}	%	N_{cores}	N_{obs}	%
-0.550	31	13	42.	17	12	71.
-0.250	45	19	42.	21	16	76.
0.050	34	24	71.	23	20	87.
0.350	31	21	68.	18	15	81.
0.650	13	13	100.	13	13	100.
0.950	4	4	100.	4	4	100.
1.250	1	0	0.	1	0	0.

for cores with positions and sizes determined by the 2D version of Clumpfind (Williams et al. 1994). We list in Table 3 our completeness statistics. Our sample includes 100% of the extinction cores with masses greater than about $3M_\odot$ with the sole exception of the star forming core Barnard 59 (Pipe-12; $M = 20M_\odot$). Between 1 and $3M_\odot$ our sample is $\sim 70\%$ complete. Below 1 M_\odot our sample includes $\sim 40\%$ of all the Alves et al. Pipe extinction cores.

Our observations of the Pipe extinction cores are spatially non-uniform. We plot in Figure 3b the 2MASS/NICER extinction map from Lombardi et al. (2006), segregating cores with and without C¹⁸O by color. For the main body of the Pipe ($DEC < -24.75^\circ$) we achieved a degree of completeness much higher than in

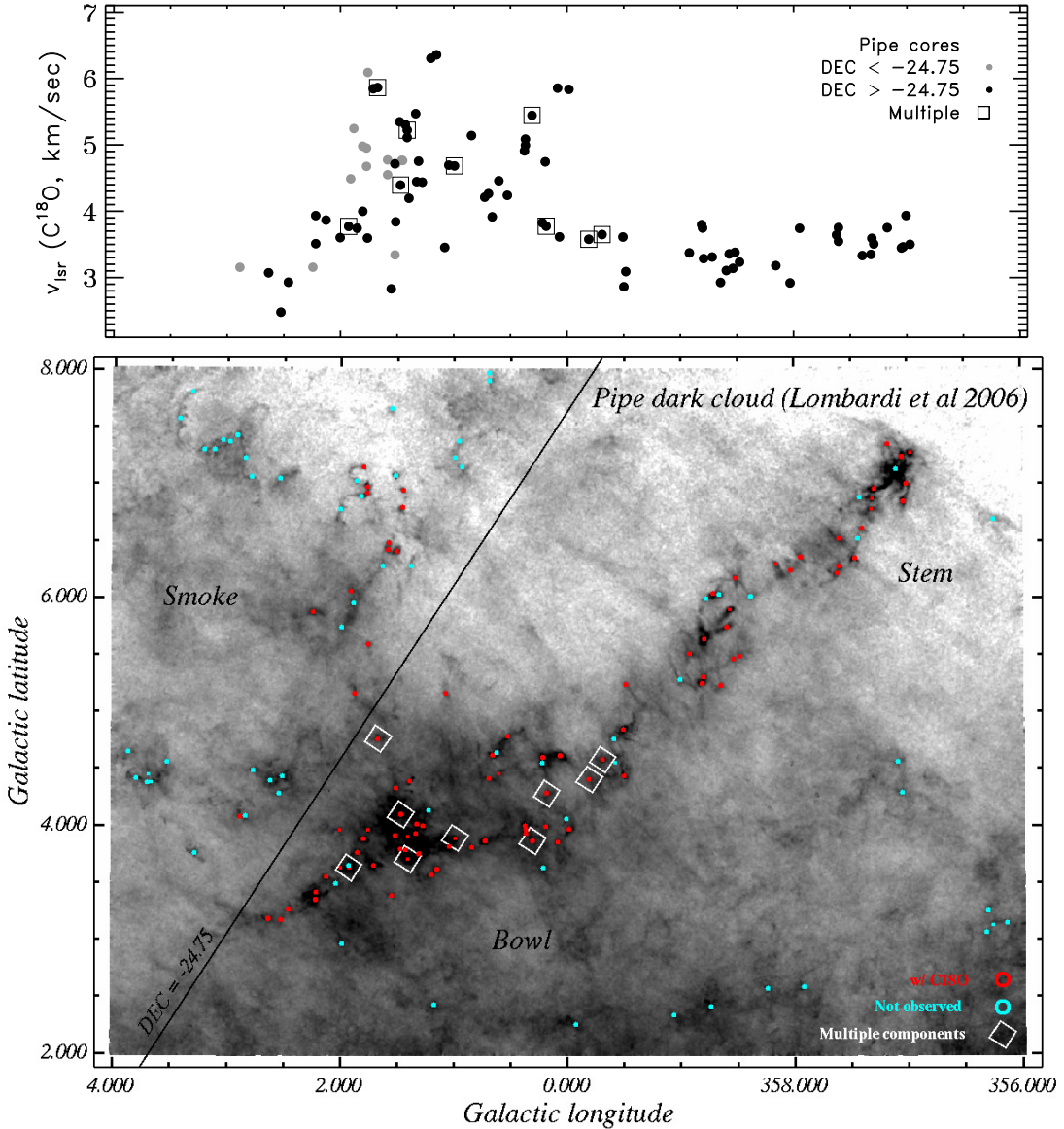


FIG. 3.— Spatial distribution of Pipe extinction cores. *Top* : Spatial variations in v_{lsr} of the Pipe cores observed in $C^{18}O$. *Bottom* : Spatial distribution of Pipe cores with and without $C^{18}O$ measurements. Underlying reverse grayscale image of the Pipe nebula in extinction (Lombardi et al. 2006). Three subregions of the Pipe referred to in text (Stem, Bowl, Smoke) and used to characterize the sample are so labeled. Sources surrounded by diamonds display multiple $C^{18}O$ line components. Bottom figure created using SAOImage DS9 (Joye & Mandel 2003).

the composite core population: $> 80\%$ for $1-3 M_{\odot}$ cores and $> 70\%$ of the subsolar mass cores. In the next section we explore the spatial homogeneity of the properties of the observed cores.

3.2. Spatial homogeneity

In this section we evaluate our sample of $C^{18}O$ observed extinction cores, comparing internally subsets of the data that are defined by their location in the cloud. Spatial subsets provide a means to evaluate our somewhat non-uniform spatial coverage; however, our spatial partitioning of the Pipe nebula is further motivated by clear physical properties of the cloud.

In panel Fig. 3a we illustrate the dependence of a core's radial velocity with Galactic longitude. The range of observed v_{lsr} , 3 to 7 km s^{-1} , is consistent with that found for $C^{18}O$ cores throughout Ophiuchus (Tachihara

et al. 2000) although we do not observe any core with $v_{lsr} < 2 \text{ km s}^{-1}$, for which Tachihara et al. observed several⁷. But unlike Ophiuchus the spatial distribution of v_{lsr} is highly structured, displaying strong correlations with Galactic longitude.

Based upon our spatial completeness and these v_{lsr} variations we divided the Pipe nebula into three regions. Each region was assigned a name that alludes to the morphology of a smoking pipe (see Fig. 3). There is a long ($4.2^{\circ}; 10 \text{ pc}$) straight (aspect ratio, $a/b \sim 3.5$) filament tracing eastward from Barnard 59 ($l, b = 357.1^{\circ}, 7.1^{\circ}$), which Barnard et al. (1927) originally called the “Sink-hole.” We will refer to this very straight filament as the “Stem” of the Pipe. The Stem displays extremely little

⁷ Two cores having $v_{lsr} > 7 \text{ km s}^{-1}$, specifically at 9 and 15 km s^{-1} do not appear on Fig. 3 and are not further examined in this work.

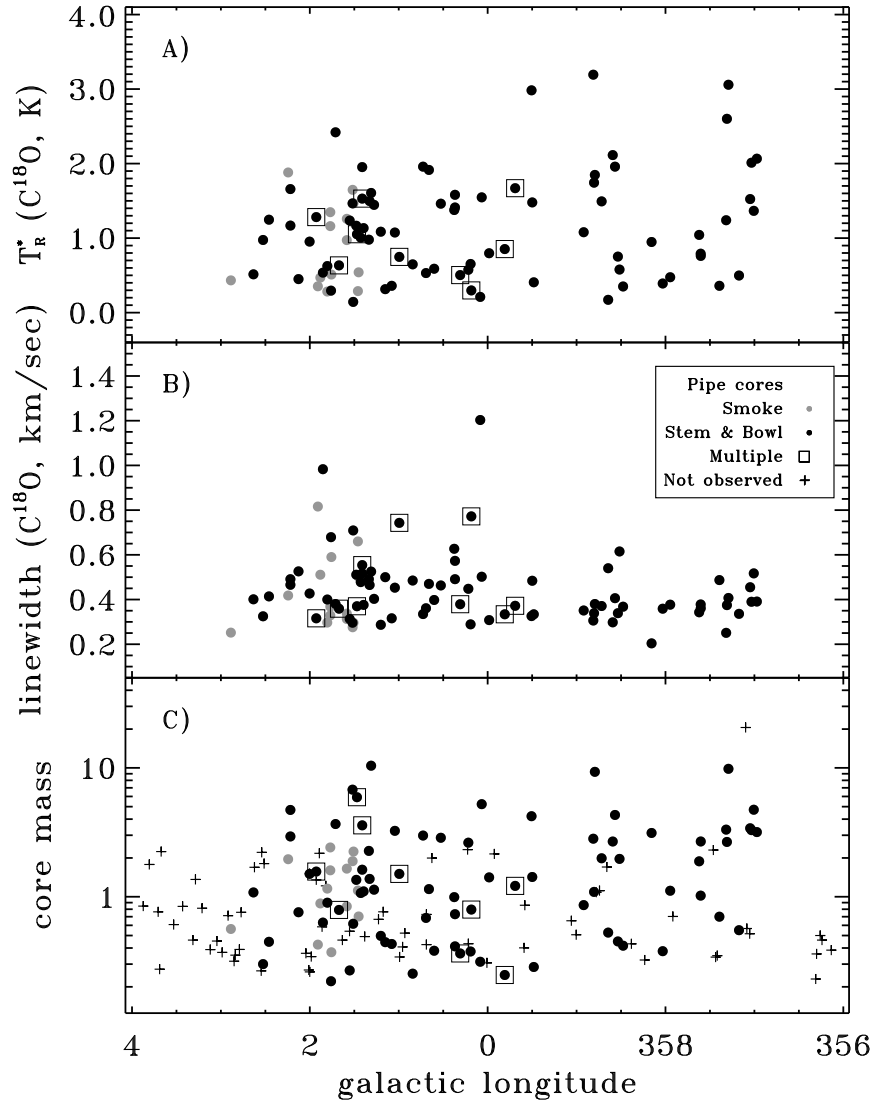


FIG. 4.— Homogeneity of core samples. Core gas and dust measurements as a function of Galactic longitude. For multiple component cores we plot the profile fit values for the “a” or brighter component.

variation in v_{lsr} of about 3.5 km s^{-1} . The Stem merges with a large dark “Bowl” at approximately $l = 0^\circ$, which is where v_{lsr} increases by 1.5 km s^{-1} , though there is larger dispersion in v_{lsr} in the Bowl compared to the Stem. Above the Bowl ($DEC < -24.75^\circ$) there are widely dispersed smaller clouds, including the dark globules of Barnard 68, 72, 74. We will call this region the “Smoke;” our C^{18}O sample is most incomplete in the Smoke. For reference the Smoke of the Pipe connects to an extinction bridge (off this map) that extends 10° northward (Dobashi et al. 2005), connecting it to the Ophiuchus main cloud.

We used two sided KS tests to determine whether these spatial samples could be drawn from the same parent. For these samples there a null possibility (10^{-8}) that the v_{lsr} distributions for the Stem and the Bowl are drawn from the same parent. The Smoke’s $v_{lsr} \sim 5 \text{ km s}^{-1}$ is very similar to and probably drawn from the same parent as the Bowl; the KS probability for the Bowl and the Smoke is 0.18. Careful inspection of Fig. 3a, however, reveals that bulk variations in v_{lsr} with position in the cloud are actually more interesting in detail than we have

examined here. In particular the increased dispersion of v_{lsr} in the Bowl is due to systematic motions (§4.1) while most of the extinction cores that we found to display multiple C^{18}O components are also found in the Bowl.

We tested the extinction cores’ remaining physical parameters ($T_R^*, \Delta v, M_{core}$) for spatial homogeneity using these subsets. In Fig. 4 we plot these three physical core parameters versus Galactic longitude. Note for simplicity the Figure only segregates the Smoke cores by symbol; Bowl cores are those with $4^\circ > l > 0^\circ$ (and $DEC > -24.75^\circ$). As can be inferred visually from Fig. 4a, the 3 Pipe regions cannot be distinguished ($P_{KS} \sim 0.3$) by the values of antenna temperature (T_R^*).

The spatial distribution of C^{18}O linewidths is shown in Fig. 4b. While the Smoke cores could have the same parent as either the Stem or the Bowl, the Stem and the Bowl have Δv distributions sufficiently different ($P_{KS} \sim 0.002$) to warrant closer inspection. Cores with multiple CO components were not used for these tests, although the test results do not change when they are included. The slight differences between the Stem and the Bowl remain even if we remove the two $\Delta v > 0.8 \text{ km s}^{-1}$

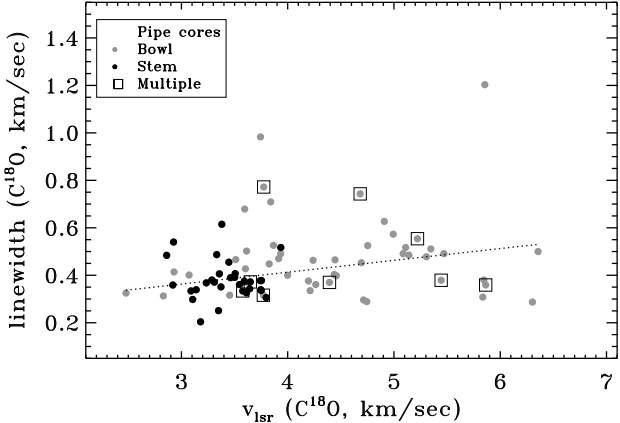


FIG. 5.— Correlation of Δv with v_{lsr} . Symbols segregated by color correspond to cores in the Stem and Bowl of the Pipe. Smoke cores are not included in this plot. Circles surrounded by squares represent the “a” component of extinction cores displaying two $C^{18}O$ components. Note the very small dispersion in the values of both v_{lsr} and Δv in the Stem. A least absolute deviation fit is shown (Table 4).

cores which could also represent unresolved double-lined components. To further explore the slight difference in linewidths between the Stem and the Bowl, we plot Δv as a function of v_{lsr} in Fig. 5. As we have shown that the Stem and the Bowl have distinct, distinguishable v_{lsr} distributions, it is not surprising that the slight differences in Δv for these two regions manifest themselves in a correlation with v_{lsr} . A linear fit suggests Δv increases by 0.05 $km\ s^{-1}$ per unit increase in v_{lsr} . As we will discuss further in §4.1.2 the larger linewidths within the Bowl are related to an interesting large scale kinematic feature of the Pipe nebula.

Interestingly, the distribution of extinction core masses along the length of the Pipe is consistent with a single parent population: $P_{KS} \sim 0.3$ when comparing the Bowl to the Stem. Further, the mass distributions for those sample of cores with $C^{18}O$ in the three regions are also indistinguishable ($P_{KS} \sim 0.1$). Moreover, the mass distribution of extinction cores that display multiple $C^{18}O$ components is basically uniform, and we confirm the vast majority of these extinction cores as real, dense cloud structures. Thus, we can conclude that the removal of such multi-component “cores” from the ensemble core mass function would not change any of the conclusions of Alves et al. (2007). In fact there is no quantity in our data that is systematically contaminated by extinction cores displaying multiple $C^{18}O$ components.

3.3. Correlations

3.3.1. Core Linewidth – Size

There is no true correlation between physical size of the Pipe extinction cores and their $C^{18}O$ linewidth (Fig. 6). A weak negative correlation ($r_c \sim -0.2$) is misleading because a least absolute deviation linear fit, which is robust against the clear outliers in this sample, reveals nothing meaningful. All fits and correlation coefficients are given in Table 4.

As we sample only the linewidth at the center of each extinction core it is perhaps meaningful to ask if the $C^{18}O$ linewidth varies on larger angular scales within the Pipe nebula. While variations of v_{lsr} on the largest

TABLE 4
CORRELATION ANALYSIS

Δv vs	Fit ^a	r_c ^b
	a0	a1
v_{lsr}	0.21	0.05
$\log r(\text{pc})$	0.43	-0.17
$\log M_{\text{core}}$	0.40	-0.15
$\log M_{\text{beam}}$	0.47	0.08

^a Result of linear least absolute deviation fit; a1 is the slope of the fit. ^b Correlation coefficient.

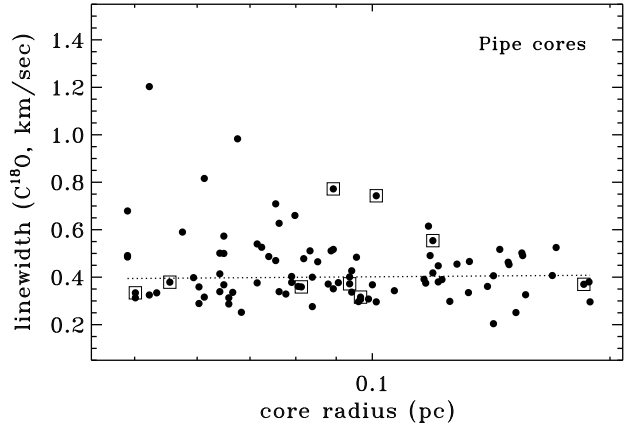


FIG. 6.— Core Linewidth – Size relation for Pipe cores. Circles surrounded by squares represent the “a” component of extinction cores displaying two $C^{18}O$ components. A least absolute deviation fit is shown (Table 4).

scales of the Pipe are discussed §4.1, we can compare our results to the integrated $C^{18}O$ linewidths data published by Onishi et al. (1999). These NANTEX data were taken with a beamwidth 3 times larger than the ARO12m and their $C^{18}O$ data correspond only to undersampled maps of ^{13}CO peaks, which miss much of the structure of the Pipe. Indeed, we find 12 NANTEX $C^{18}O$ cores contain 20 extinction cores. In 8 cases where a single NANTEX core contains only 1-2 extinction cores we find that an additional linewidth component of order the linewidth of an individual extinction core is needed to recover the larger scale integrated linewidth. Determining whether this additional component comes from organized v_{lsr} variations in the gas or from general inter-core turbulence requires fully sampled maps. We do note that in a few cases where we have measurements for multiple extinction cores per NANTEX core, v_{lsr} variations between cores within the NANTEX beam are sufficient to explain these differences.

3.3.2. Core Linewidth – Mass

In this section we explore the dependence of the $C^{18}O$ linewidth on the mass of the individual Pipe extinction cores. We use the mass of each Pipe extinction core as derived from the wavelet analysis of the extinction map, which effectively subtracts away the diffuse cloud in which the core is enveloped. As is clear in Fig. 7a there is no positive correlation between a cores mass and its linewidth as would be expected if the cores are in a state of virial equilibrium. As was the case for the linewidth-size relation the scatter in this diagram might suggest mass and linewidth are negatively correlated since larger

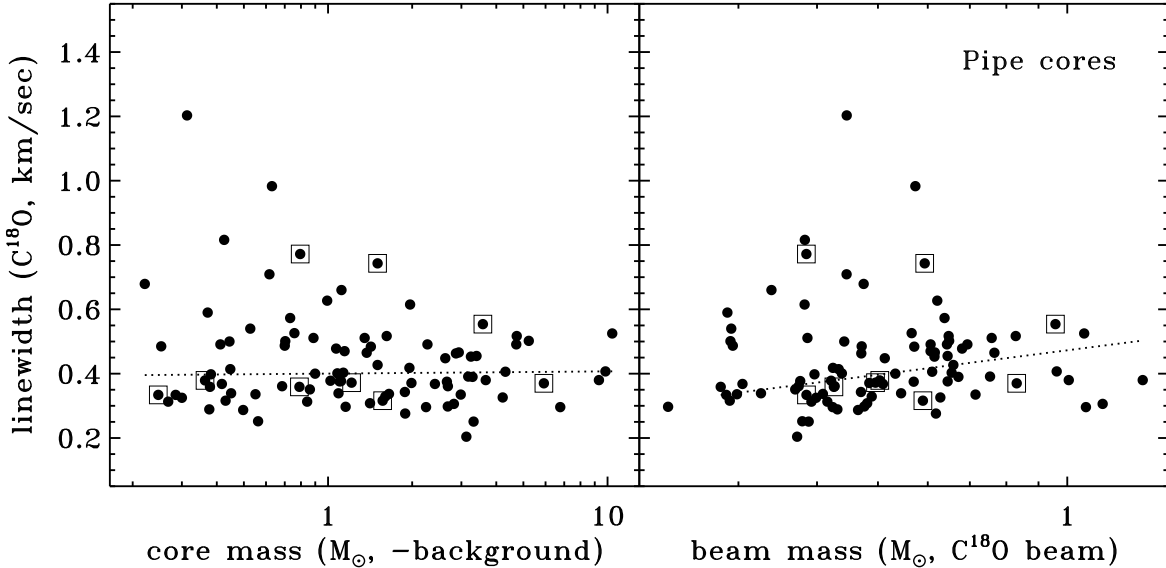


FIG. 7.— Core Linewidth – Mass relations for the Pipe. *Left* : Linewidth is plotted as a function of core mass, derived from the wavelet subtracted map of Alves et al. (2007) and tabulated in Lada et al. (2007). *Right* : Linewidth is plotted as a function of the integrated column density seen by the radio beam and expressed in mass units. Beam fluxes given in Table 2. Circles surrounded by squares represent the “a” component of extinction cores with two C¹⁸O components. A least absolute deviation fit is shown (Table 4).

linewidths are more frequently observed for less massive ($< 1 M_{\odot}$) cores. But such an inference is due primarily to outliers as our linear fit shows no correlation.

It may not be reasonable to assume that the linewidth at the extinction peak should correlate with core mass. The C¹⁸O beam traces the entire column density along the line of sight which would include any contribution from the inter-core material whose mass is not reflected in Fig. 7a because the background was removed by the wavelet analysis. Further, for 75% of the Pipe cores the C¹⁸O beam subtends less than 20% of the area of the extinction core. Perhaps it is more precise to ask if the linewidth correlates with the observed column density in the AR012m beam (56'') as determined from the 2MASS/NICER extinction map without subtracting for background. Using wphot in IRAF we measured the total flux expressed in A_V within a Gaussian weighted beam having a 56'' FWHM and summed to 3σ ($R = 71''$). Table 2 is supplemented with these fluxes. In Fig. 7b we convert this flux to mass⁸ and compare it to the linewidth. A linear fit suggests that linewidth is more correlated to central beam mass than core mass. This could suggest that extinction cores that find themselves embedded in larger cloud envelopes have slightly larger linewidths than those cores which are isolated. Because ammonia observations that tracer higher density gas confirm the lack of linewidth variations with the cores’ size (Rathborne et al. 2007), we instead believe that our C¹⁸O data is picking up non-negligible emission from inter-core gas.

4. DISCUSSION

4.1. Large scale kinematics of the Pipe nebula

⁸ The conversion from total column density as measured in magnitudes of extinction (A_V) is $0.00757 M_{\odot}/mag$. This constant is derived assuming a distance of 130 pc (Lombardi et al. 2006), using a size of 30'' per pixel in the extinction map, and employing the basic atomic and astrophysical constants as given by Cox (2000).

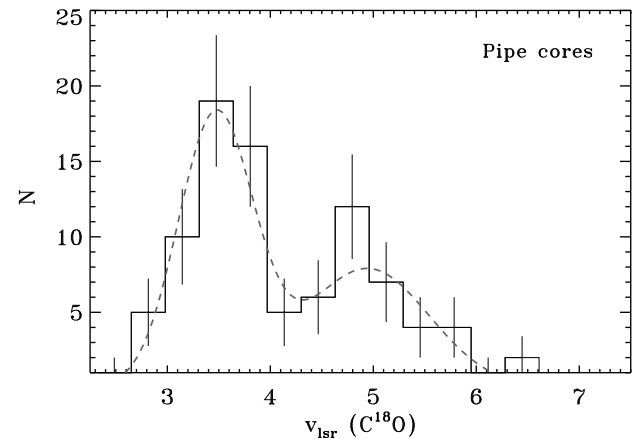


FIG. 8.— v_{lsr} distribution function for the Pipe C¹⁸O cores. Two component Gaussian profile fit is shown; see text.

In this section we examine the large scale kinematics of the Pipe nebula. As was clear in Fig. 3, the dense extinction cores in the molecular cloud display strong spatial v_{lsr} variations. The v_{lsr} distribution function (Fig. 8) of these cores allows us to broadly characterize the Pipe nebula’s *dense* core kinematics, which appear to consist of 2 components. Fitting these components as Gaussian distributions yield central velocities of $v_{lsr,1} = 3.48$ and $v_{lsr,2} = 4.95 \text{ km s}^{-1}$ with corresponding dispersions of $\sigma(v_1) = 0.37$ and $\sigma(v_2) = 0.55 \text{ km s}^{-1}$.

Using the v_{lsr} distribution function for the dense extinction cores as a guide, the global kinematic structure of the Pipe cloud becomes very evident in the ¹³CO channel maps of Onishi et al. (1999). Overlaying two channel maps centered at 3.5 and 5 km s⁻¹ on to our extinction map in Fig. 9, we show that these two components are clearly spatially organized: the primary component of the Pipe is a 15 pc long filament centered at $v_{lsr} \sim 3.5 \text{ km s}^{-1}$ and stretching (7°) across our entire field of view. Surprisingly, this main component is narrow both physically and kinematically, especially in

TABLE 5
REGIONAL CLOUD AND CORE EXTINCTION PROPERTIES

Region	N_{Pixels}	Cloud ^a Total Flux (ΣA_V ; mag)	Mass (M/M_\odot)	N_{core}	Cores ^b ΣM_{total} (M/M_\odot)	ΣM_{bcksb} (M/M_\odot)
Stem	68621	196012	1500	53	208	102
Bowl	83498	410748	3100	57	308	95
Ring ^c	24519	147437	1100	37	230	70
Smoke	146272	367895	2800	49	106	47

^a Cloud extinction properties derived from total extinction map of Lombardi et al. (2006) without subtraction for background. One pixel has an angular size of $30''$. Although the regions are not circular an effective radius for each region can be calculated as $0.01 \cdot \sqrt{N_{Pixels}}$ pc, assuming a distance of 130 pc (Lombardi et al. 2006). ^b Core masses derived by summing individual extinction core masses as listed in Alves et al. (2007) without subtraction for the background cloud (ΣM_{total}) and after wavelet subtraction of the background (ΣM_{bcksb} ; Lada et al. 2007).^c Note, the Ring region is enclosed by the Bowl.

the Stem of the Pipe. As it twists around one side of the Bowl the main component is somewhat redshifted ($v_{lsr} \sim 4 \text{ km s}^{-1}$) relative to the Stem but shifts back to 3.5 km s^{-1} for $l > 1.5^\circ$ (see also Fig. 3a). The molecular material of the 5 km s^{-1} component is concentrated in a coherent feature within Bowl that parallels the slightly redshifted portion of the main component. It overlaps the 3.5 km s^{-1} component at $l = 0^\circ$ and $l = 1.5^\circ$, forming an apparent “ring” in the Bowl. We now explore more closely the kinematics of each portion of the Pipe.

4.1.1. Kinematics of the Stem

As was clear in Fig. 5 the Stem of the Pipe displays a very different kinematic signature than the Bowl; specifically, the extinction cores in the Stem display smaller dispersions in *both* linewidth and v_{lsr} . The Stem consists of a single well organized very linear structure. For Stem cores with C^{18}O data, we can fit the v_{lsr} distribution function with a single component, which is narrower even than the 3.5 km s^{-1} component fit in Fig. 8. Over its 10 parsec length the dense cores in the Stem display a core to core standard deviation, $\sigma(v_{lsr})$, of only 0.27 km s^{-1} . On the one hand the core to core motions in the Stem are slightly larger than the sound speed (0.2 km s^{-1} at 10K)⁹. On the other hand the gas contained within the Stem cores is subsonic; the median 1 dimensional C^{18}O velocity dispersion for the gas within a dark extinction core in the Stem is $\sigma_{1d} = 0.16 \text{ km s}^{-1}$ ($\Delta v = 0.38 \text{ km s}^{-1}$) with a variance of 1.3×10^{-3} . Summing these gas motions, i.e., $\sigma(v_{lsr})$ and σ_{1d} , in quadrature, we derive a total 1-dimensional velocity dispersion for C^{18}O in the Stem of 0.32 km s^{-1} or 0.56 km s^{-1} in 3 dimensions (σ_{3d}). Again this is not much larger than the 3-dimensional sound speed of molecular hydrogen (0.35 km s^{-1}). Moreover, it is significantly smaller than those values typical for 10 parsec structures as derived by Larson (1981). Those structures display $\sigma_{3d} \sim 2.5 \text{ km s}^{-1}$.

Larson had commented that on these (10pc) physical scales large scale v_{lsr} gradients contribute significantly to σ_{3d} . By eye any gradient of v_{lsr} with Galactic longitude (Fig. 3a) appears quite small; a linear fit yields a gradient of $|\delta v_{lsr}| \sim 0.1 \pm 0.1 \text{ km s}^{-1}\text{deg}^{-1}$. The bulk motion of the gas along the Stem appears much more or-

ganized than in those clouds described by Larson. An alternate source for such a missing and substantially larger non-thermal component could be the lower density core and cloud envelopes. Our analysis of C^{18}O on different size scales (§3.3.1) suggests any “additional” non-thermal linewidth can only be of order the typical linewidth, raising σ_{3d} insignificantly. To examine gas at large scales and lower densities we summed the Onishi et al. ^{13}CO line over the Stem; this experiment yields a total ^{13}CO linewidth of $\sim 1 \text{ km s}^{-1}$ or $\sigma_{3d} \sim 0.7 \text{ km s}^{-1}$. We conclude that our observations of the dark extinction cores in the Stem of the Pipe are tracing the dense portions of a cloud in a different physical state than characterized by clouds studied by Larson.

4.1.2. The Bowl and a Ring

The Bowl is clearly composed of molecular gas from the two main velocity components and it appears that these two velocity components trace a large coherent ring-like (in projection) structure of molecular material in the Bowl. We believe that the Pipe Molecular Ring is not a shell because there are neither dense extinction cores nor significant ^{13}CO emission at any velocity at the center of the Ring. Although the two components can be seen clearly in the ^{13}CO data cube of Onishi et al. (1999), the existence of multiple components in the Pipe was discussed only briefly by Onishi et al. who noted three C^{18}O cores at the eastern end of the Ring that overlapped spatially but had differing values of v_{lsr} .

At $v_{lsr}=4.5 \text{ km s}^{-1}$ the Pipe Molecular Ring forms a projected ellipse in ^{13}CO with maximum spatial dimensions of 4.7 pc by 2.9 pc and an effective radius ($= \sqrt{(\text{area}/\pi)}$) of 2.1 pc . Its total mass is $\sim 1100 M_\odot$ (Tab. 5), which was calculated from the Lombardi et al. (2006) 2MASS extinction map and excludes the flux of the central hole having a radius $\sim 1 \text{ pc}$ and a mass of $150 M_\odot$. Alves et al. identified 37 dark extinction cores in this Ring; these dense cores comprise $\sim 6\%$ of the total Ring mass. We observed 32 of them in C^{18}O .

The ballistics of the dense extinction cores as determined from our C^{18}O observations permit us to further investigate the nature of this Ring. Taken as an ensemble the maximum radial velocity difference for the Ring cores is 2.2 km s^{-1} with $\sigma(v_{lsr}) = 0.61 \text{ km s}^{-1}$. These core to core motions are (very) large relative to the motions of cores in the Stem (Fig. 3) and are due at least in part to the systematic nature of v_{lsr} variations around

⁹ Rathborne et al. (2007) found a typical kinetic temperature of $12 \pm 2 \text{ K}$ using ammonia measurements of a sample of these Pipe cores.

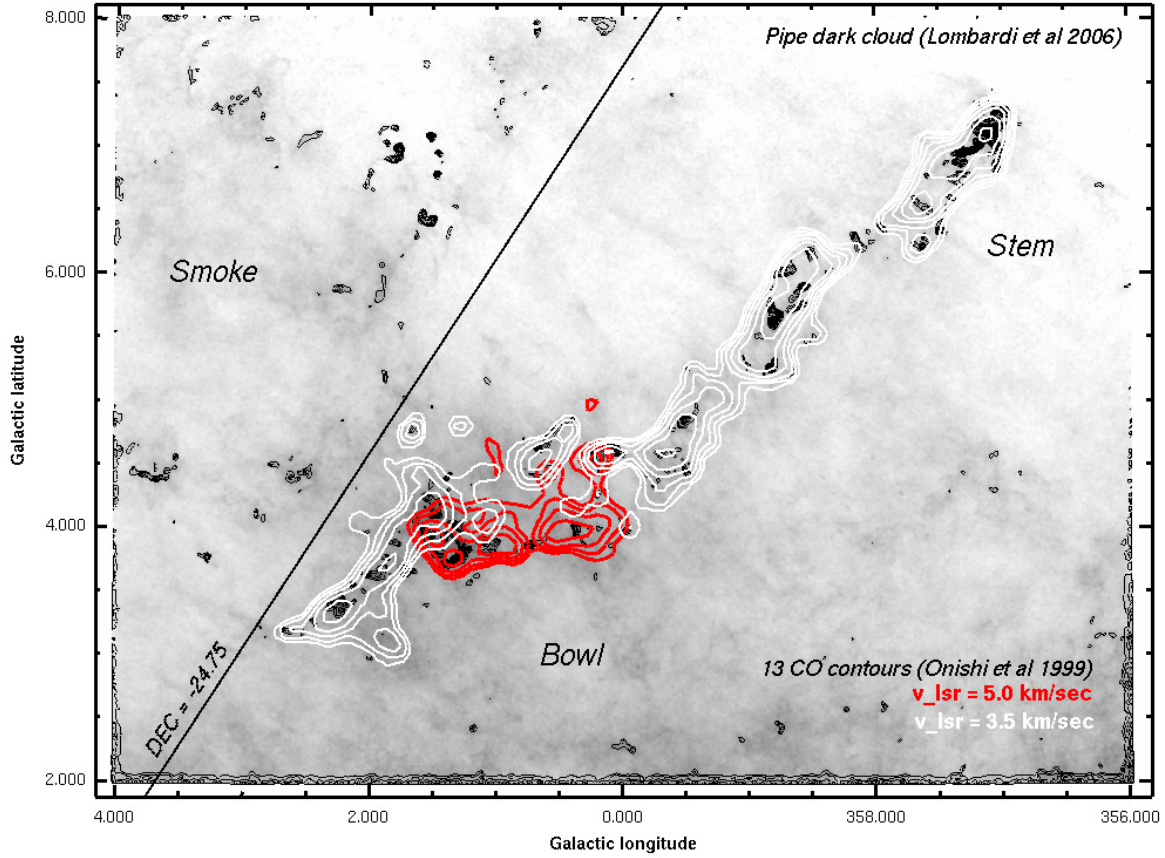


FIG. 9.— Smoothed ^{13}CO channel maps at 3.5 (white) and 5.0 (red) km s^{-1} , illustrating the two primary velocity components of the Pipe nebula (data from Onishi et al. 1999). These components trace the large scale kinematic feature we refer to as the Pipe Molecular Ring. Black contours correspond to the wavelet subtracted map of Alves et al. (2007) overplotted on the complete 2MASS extinction map (inverted grayscale). This figure was created using SAOImage DS9 (Joye & Mandel 2003).

TABLE 6
RING C¹⁸O PROPERTIES

Quadrant	N_{core}	$\langle v_{\text{lslr}} \rangle$	$\sigma(v_{\text{lslr}})$	$\langle \sigma_{1d} \rangle$
180 \rightarrow 90	6	4.05	0.29	0.19
90 \rightarrow 0	2	4.02	0.18	0.23
0 \rightarrow -90	12	5.17	0.61	0.20
-90 \rightarrow -180	7	5.09	0.54	0.23
North	8	4.04	0.27	0.20
South	19	5.14	0.59	0.21

NOTE. — All velocity dispersions given in units of km s^{-1} .

the Ring. These core motions are not, however, sufficient for them to escape the gravitational field of the ring ($v_{\text{esc}} \sim 2.35 \text{ km s}^{-1}$). After projecting the locations of the cores into polar coordinates¹⁰, we plot the values of v_{lslr} versus angle, θ , which places us in the reference frame of the Ring and traces angularly the Ring's circumference (Fig. 10)¹¹. First, we can see that the dense cores are not behaving as a rotating ring, which would trace a parabola in this Figure. There are instead strong gradients in v_{lslr} at $\theta = 0^\circ$ and $\theta = -180^\circ$. The cores in

the northern half of the Ring ($\theta > 0$) are only somewhat redshifted relative to the main cloud ($v_{\text{lslr}} = 4 \text{ km s}^{-1}$) while their localized core to core motions are similar to the Stem ($\sigma(v_{\text{lslr}}) \sim 0.27 \text{ km s}^{-1}$; Table 6).

The extinction cores in the southern half of the ring are clearly centered on the 5 km s^{-1} cloud component. However, they display radial velocity variations ($\sigma(v_{\text{lslr}}) \sim 0.6 \text{ km s}^{-1}$) that do not appear to be related to the overall Ring structure and are much larger than in the northern half. To better illustrate these motions we plot in Figure 11 a ^{13}CO position-velocity diagram aligned with this part of the Ring ($\theta < 0^\circ$). Note, this $l - v$ diagram is integrated over an 0.6° wide band centered at approximately $b = 3.9^\circ$. In ^{13}CO we observe a rapid but systematic transition from the 3.5 km s^{-1} to the 5 km s^{-1} clouds at $l = 1.5^\circ$. Along the extent of the 5 km s^{-1} component we observe large variations in the lower density gas, ranging from 4 to 6.5 km s^{-1} , and mirrored by the kinematics of the denser cores. In addition to cores at 5 km s^{-1} there appears to be gas with dense cores clustered at 6.3 km s^{-1} as well as at least one core at 4 km s^{-1} .

When we perform the same experiment for the Pipe Molecular Ring as for the Stem and average the ^{13}CO data for the Bowl, we find $\sigma_{3d} \sim 1.8 \text{ km s}^{-1}$, substantially larger than the Stem. As we have shown most of this dispersion comes from the systematic velocity differ-

¹⁰ Projection centered $(l, b)_0 = (0.755^\circ, 4.172^\circ)$

¹¹ Note, $\theta = 0^\circ$ corresponds to increasing Galactic longitude (East); 90° is increasing Galactic latitude (North); $\pm 180^\circ$ corresponds to where the base of the Stem and the Ring meet (West, $l \sim 0^\circ$)

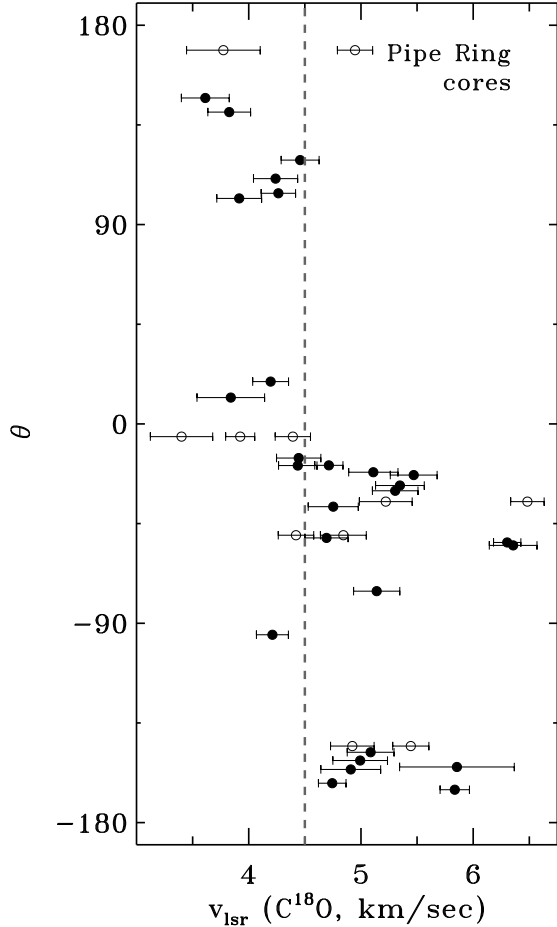


FIG. 10.— Variations in radial velocity within the Pipe Molecular Ring as traced by the C^{18}O data of the dark extinction cores (circles). Unfilled circles correspond to cores with multiple C^{18}O components; the v_{lsr} of each component is shown. The 1σ dispersion in C^{18}O is overplotted for each point. The dashed line at $v_{lsr} = 4.5 \text{ km s}^{-1}$ corresponds approximately to that velocity where emission from ^{13}CO can be seen around the entire ring. The projection to polar coordinates was performed centering on $(l, b)_0 = (0.755^\circ, 4.172^\circ)$. The axis of increasing Galactic longitude (East) corresponds to 0° ; 90° is increasing Galactic latitude (North); 180° corresponds to where the base of the Stem and the Ring meet (West, $l \sim 0^\circ$).

ence between the two components ($\Delta v_{lsr} = 1 \text{ km s}^{-1}$) and from the larger core to core motions in the Ring ($\sigma(v_{lsr}) \sim 0.6 \text{ km s}^{-1}$). Yet it is also important to notice that cores all around the Ring display linewidths elevated (0.48 km s^{-1}) relative to the Stem (0.38 km s^{-1}) or any other part of the Pipe cloud (Tab. 6).

It is not clear whether the Ring is a single coherent feature or a superposition of two independent filaments, one of which (the $\sim 5 \text{ km s}^{-1}$ portion) is substantially clumpier than the other. We can say that the extinction cores in the northern portion of the Ring differ from the main 3.5 km s^{-1} cloud in that they are redshifted slightly and display slightly larger linewidths. Even if these facts point to a physical association for the two sides of the Ring, we cannot infer the line of sight geometry for this complicated region and cannot precisely ascertain an origin for these kinematics. The net velocity difference ($\Delta v_{lsr} \sim 1 \text{ km s}^{-1}$) between the two sides of the Ring may be the signature of either a collapse or an expansion, though it does constrain the region's evo-

lutionary timescale to be of order 2 Myr. Thus, either case could correspond to a primordial kinematic feature from the creation of the cloud. We prefer a primordial explanation because the cores of the Ring appear bound to it, and we think it unlikely that the cloud has been modified by some localized but external event. The kinetic energy of the ring is of order 10^{46} ergs, which is too small to suggest the influence of a nearby supernovae. Such an event would likely have also similarly impacted a much larger portion of the cloud. Onishi et al. (1999) examined the possible influence of nearby B stars, finding them too distant to affect any portion of the Pipe except Barnard 59, which is $\sim 5^\circ$ away.

We can further compare the Pipe Molecular Ring¹², to physical structures found in the Taurus molecular cloud. There are two features in Taurus that have received attention as apparent rings: Heiles Cloud 2 (HCl2) (Schloerb & Snell 1984; Cernicharo & Guelin 1987) and Barnard 18 (Murphy & Myers 1985). Both clouds have masses ($10^3 M_\odot$), radii (1-2pc) and internal velocity differences ($1-2 \text{ km s}^{-1}$) similar to the Pipe. HCl2 has an obvious ring-like structure in the extinction map of Padoan et al. (2002) (see also Tóth et al. 2004), while Barnard 18 is primarily a weak kinematic structure without strong CO or extinction signatures. Moreover, the kinematics of HCl2 are much more similar to those we find in the Pipe Molecular Ring, displaying complicated signatures of overlapping filaments that do not trace a rotating ring (Cernicharo & Guelin 1987).

To speculate on an origin for such structures it is important to recognize a fundamental difference between the Pipe and Taurus, namely the present day star formation rate. The Taurus cloud likely represents a more evolved star forming analogue to the Pipe nebula; indeed, both of the rings in Taurus contain young stars. In fact Murphy & Myers suggested that Barnard 18 is an expanding ring caused by a small group of ~ 10 stars projected near its center (Myers 1982). As illustrated by Tóth et al. (2004) the HCl2 ring contains star formation on at least two sides, including a Class I protostar in TMC-1 and IRAS point sources in IC 2087. The Pipe Molecular Ring is apparently free of any present day star formation. Onishi et al. (1999) found no IRAS point sources within the Pipe Molecular Ring that have the colors of YSOs and our visual inspection of IRAS scans and optical DSS plates indicate to us that there are *neither* IRAS sources of any color nor bright DSS sources that could be B stars in this Ring. Simply, there do not appear to be any young stars in or near the Ring whose outflows would be responsible for its kinematics. We find that the existence of the Pipe Molecular Ring sans young stars supports a hypothesis that such ring-like structures are likely primordial, resulting from the creation of the cloud.

4.1.3. The Smoke

Most of the Smoke extinction cores we observed with C^{18}O are in fact members of the 5 km s^{-1} component, though a full discussion of spatial variations in v_{lsr} in the Smoke is limited by our spatial incompleteness. Ex-

¹² We so name this apparent feature to reflect its similarities to the Taurus Molecular Ring, a moniker given to HCl2 in the literature.

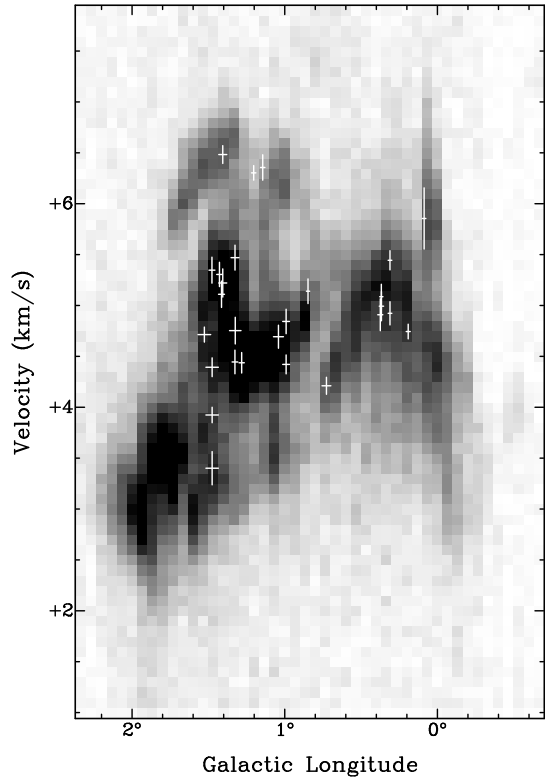


FIG. 11.— Variations in radial velocity along the Pipe Molecular Ring traced using the ^{13}CO data of Onishi et al. (1999). This figure is the ^{13}CO Galactic longitude-velocity diagram (l, v) averaged over a 0.6° band centered at $b = 3.9^\circ$. It corresponds to the ^{13}CO gas enveloping those cores with negative values of θ in Fig. 10. The extinction cores in this part of the Ring are overplotted as crosses, using their $\text{C}^{18}\text{O } v_{lsr}$. The crosses have widths in l, v corresponding to the extinction core's radius and C^{18}O linewidth.

cluding three cores that are in the 3 km s^{-1} component, the remaining 9 C^{18}O cores have $v_{lsr} = 4.8 \text{ km s}^{-1}$ with $\sigma(v_{lsr}) = 0.2 \text{ km s}^{-1}$, which is smaller even than the Stem. The extinction cores in the Smoke have uniformly narrow linewidths, with a median $\Delta v = 0.4$ ($\sigma = 0.14$) km s^{-1} ; their total $\text{C}^{18}\text{O } \sigma_{3d} = 0.4 \text{ km s}^{-1}$ with similar spatial dimensions as the Stem albeit with a different projected geometry. As was the case for the Bowl, the Alves et al. (2007) cores constitute only 2% of the total column density in the Smoke (Table 5). Indeed, most of the mass for the Smoke is in very diffuse gas; 2/3 of the total Smoke mass is in regions with $A_V < 2$ mag. Interestingly, there is no core in the Smoke with a mass greater than $2\mathcal{M}_\odot$.

A discussion of a few of the Smoke extinction cores is warranted. Barnard 68 (Pipe-101) and Barnard 72 (aka, “the Snake,” Pipe-111 and 112; GF 1 Schneider & Elmegreen (1979)) can be seen at $l = 2^\circ$; $b = 7^\circ$ in Figs. 3 & 9. These dark extinction cores have a striking, dark appearance at optical wavelengths, which has led to their frequent appearance in astrophotographs. These cores are separated angularly by about $17'$ but they are separated in velocity by 1.5 km s^{-1} (3.36 vs 4.96 km s^{-1}). Further observations will be valuable to determine how the velocities of cores in the Pipe’s Smoke are spatially distributed.

5. CONCLUSIONS

We have used the ARO12m radio telescope to characterize the molecular gas properties of the dark extinction cores identified by Alves et al. (2007) in the near-IR extinction map derived by Lombardi et al. (2006). We obtained central pointings for 94 dark extinction cores in $\text{C}^{18}\text{O } J=1-0$ line at an angular resolution optimally matched to the resolution of the extinction map. All the cores were detected in C^{18}O and less than 10% of the cores display multiple velocity components. This confirms that most of the extinction cores in the Pipe are true dense cores and are not the superposition of unrelated filaments. We find no correlations between the derived molecular linewidths of C^{18}O and the properties (R, M) of these dark extinction cores. These non-correlations are confirmed by higher density ammonia observations (Rathborne et al. 2007) and interpreted by Lada et al. (2007) as evidence that the cores of the Pipe are thermally supported and in pressure equilibrium with the external cloud.

While we find no correlation between basic core properties and the molecular C^{18}O linewidth we do find a strong correlation between a Pipe extinction core’s radial velocity and its location in the cloud. We find that there are two well defined velocity components of the molecular gas in the Pipe. One is primarily located in a very narrow spatial feature that stretches 15pc across the region and it characterized by a small dispersion in radial velocity. Its internal kinematics and gas motions are inconsistent with the relations derived by Larson (1981) for large turbulent gas clouds. The second component forms half of an apparent ring within the Bowl of the Pipe, having a radius of ~ 2 pc and a mass of $\sim 1000\mathcal{M}_\odot$. The extinction cores in the Pipe Molecular Ring have linewidths somewhat elevated relative those cores in the main cloud component. The lower density ^{13}CO gas displays far larger motions than similar gas of the main component. Unlike similar rings in Taurus, there are no apparent young stars in the Pipe Molecular Ring that could be modifying the cloud cores’ kinematics. Thus, both the Stem of the Pipe and the Pipe Molecular Ring appear to be primordial features of this young dark cloud. In summary we find the kinematics of the Pipe cloud to be relatively quiescent over most of its 15 pc length having subsonic C^{18}O extinction cores and displaying core to core motions only somewhat larger than the sound speed. The mostly systematic nature of motion in the Pipe Molecular Ring warrants further detailed study through spatially complete mapping of C^{18}O as well as molecular line transitions that trace higher densities.

We extend our appreciation to the staff of the Arizona Radio Observatory for supporting our observations and scheduling ample observing time. The Kitt Peak 12 Meter is operated by the Arizona Radio Observatory (ARO), Steward Observatory, University of Arizona. We further thank T. Onishi for access to the ^{13}CO cube of the Pipe. An anonymous referee provided comments that improved parts of this paper. This research made use of IDL procedures developed and publicly available from C. Markwardt. This research made use of SAOImage DS9, developed by Smithsonian Astrophysical Observa-

tory (Joye & Mandel 2003). This research was supported in part by NASA Origins grant NAG10341 and NASA

Spitzer grant.

Facilities: Arizona Radio Observatory Kitt Peak 12m

REFERENCES

- Alves, J., Lombardi, M., & Lada, C. J. 2007, A&A, 462, L17
 Alves, J. F., Lada, C. J., & Lada, E. A. 2001, Nature, 409, 159
 Barnard, E. E., Frost, E. B., & Calvert, M. R. 1927, A photographic atlas of selected regions of the Milky way ([Washington] Carnegie institution of Washington, 1927.)
 Brooke, T. Y., Huard, T. L., Bourke, T. L., Boogert, A. C. A., Allen, L. E., Blake, G. A., Evans, II, N. J., Harvey, P. M., Koerner, D. W., Mundy, L. G., Myers, P. C., Padgett, D. L., Sargent, A. I., Stapelfeldt, K. R., van Dishoeck, E. F., Chapman, N., Cieza, L., Dunham, M. M., Lai, S.-P., Porras, A., Spiesman, W., Teuben, P. J., Young, C. H., Wahhaj, Z., & Lee, C. W. 2007, ApJ, 655, 364
 Cambrésy, L. 1999, A&A, 345, 965
 Cernicharo, J. & Guélin, M. 1987, A&A, 176, 299
 Cox, A. N. 2000, Allen's astrophysical quantities, ed. A. N. Cox (Allen's astrophysical quantities, 4th ed. Publisher: New York: AIP Press; Springer, 2000. Edited by Arthur N. Cox. ISBN: 0387987460)
 Dobashi, K., Uehara, H., Kandori, R., Sakurai, T., Kaiden, M., Umemoto, T., & Sato, F. 2005, PASJ, 57, 1
 Kutner, M. L., & Ulrich, B. L. 1981, ApJ, 250, 341
 Goodman, A. A., Barranco, J. A., Wilner, D. J., & Heyer, M. H. 1998, ApJ, 504, 223
 Joye, W. A. & Mandel, E. 2003, in Astronomical Society of the Pacific Conference Series, Vol. 295, Astronomical Data Analysis Software and Systems XII, ed. H. E. Payne, R. I. Jedrzejewski, & R. N. Hook, 489–
 Lada, C. J., Lada, E. A., Clemens, D. P., & Bally, J. 1994, ApJ, 429, 694
 Lada, C. J., Muench, A. A., Rathborne, J., Alves, J. F., & Lombardi, M. 2007, ApJ, submitted
 Larson, R. B. 1981, MNRAS, 194, 809
 Lee, C. W., & Myers, P. C. 1999, ApJS, 123, 233
 Lee, C. W., Myers, P. C., & Tafalla, M. 1999, ApJ, 526, 788
 —, 2001, ApJS, 136, 703
 Lombardi, M. & Alves, J. 2001, A&A, 377, 1023
 Lombardi, M., Alves, J., & Lada, C. J. 2006, A&A, 454, 781
 Motte, F., Andre, P., & Neri, R. 1998, A&A, 336, 150
 Murphy, D. C. & Myers, P. C. 1985, ApJ, 298, 818
 Myers, P. C. 1982, ApJ, 257, 620
 Onishi, T., Kawamura, A., Abe, R., Yamaguchi, N., Saito, H., Moriguchi, Y., Mizuno, A., Ogawa, H., & Fukui, Y. 1999, PASJ, 51, 871
 Padoa, P., Cambrésy, L., & Langer, W. 2002, ApJ, 580, L57
 Rathborne, J., Lada, C. J., Muench, A. A., Alves, J. F., & Lombardi, M. 2007, ApJ, submitted
 Reipurth, B., Nyman, L.-A., & Chini, R. 1996, A&A, 314, 258
 Schloerb, F. P. & Snell, R. L. 1984, ApJ, 283, 129
 Schneider, S. & Elmegreen, B. G. 1979, ApJS, 41, 87
 Tachihara, K., Mizuno, A., & Fukui, Y. 2000, ApJ, 528, 817
 Tóth, L. V., Haas, M., Lemke, D., Mattila, K., & Onishi, T. 2004, A&A, 420, 533
 Williams, J. P., de Geus, E. J., & Blitz, L. 1994, ApJ, 428, 693
 Wolf, M. 1923, Astronomische Nachrichten, 219, 109

TABLE 7
C¹⁸O DATA

Pipe (ID)	flag (a)	Position (J2000)		r_{sep} (")	v_{lsr} (km s ⁻¹)	dv	T_R^* (K)	rms	$\Sigma A_V^{(b)}$ (mag.)
6		17:10:31.01	-27:25:33.31	8.07	3.501	0.391	2.066	0.06	99.6
7		17:11:36.39	-27:33:50.70	19.97	3.935	0.517	1.366	0.05	85.6
8		17:12:15.04	-27:37:44.41	2.76	3.462	0.390	2.012	0.05	88.7
11		17:10:49.87	-27:23:04.07	6.06	3.446	0.455	1.524	0.07	85.2
13		17:10:47.22	-27:13:41.43	9.64	3.751	0.336	0.498	0.05	39.4
14		17:12:31.40	-27:21:26.02	3.82	3.506	0.407	3.058	0.06	127.1
15		17:12:52.20	-27:23:29.87	2.64	3.591	0.375	2.601	0.08	75.3
16		17:13:14.81	-27:25:45.25	31.95	3.349	0.251	1.240	0.11	51.2
17		17:14:04.72	-27:28:02.65	33.32	3.332	0.487	0.360	0.03	38.8
20		17:15:13.95	-27:33:20.50	60.61	9.144	0.348	1.296	0.21	65.3
21		17:14:55.99	-27:21:31.59	4.85	3.546	0.361	0.761	0.11	49.4
22		17:15:47.79	-27:29:34.63	5.87	3.753	0.378	0.791	0.09	55.6
23		17:16:05.39	-27:30:54.57	2.62	3.642	0.343	1.043	0.06	62.1
25		17:16:22.70	-27:10:15.51	18.40	3.742	0.377	0.475	0.09	49.7
26		17:17:00.81	-27:10:01.52	22.83	2.919	0.359	0.391	0.04	37.1
27		17:17:08.56	-27:01:54.20	4.49	3.180	0.204	0.948	0.09	49.1
30		17:20:58.21	-27:13:32.25	21.67	3.234	0.368	0.351	0.03	40.2
31		17:18:30.79	-26:48:39.96	15.90	3.380	0.615	0.578	0.07	50.5
32		17:21:12.09	-27:11:26.84	25.90	3.139	0.339	0.752	0.03	43.0
33		17:19:40.34	-26:55:38.55	16.35	3.357	0.406	1.959	0.05	80.5
34		17:20:17.69	-26:59:22.48	12.20	3.106	0.298	2.114	0.06	62.8
35		17:22:20.45	-27:14:35.63	20.13	2.926	0.540	0.172	0.03	38.6
37		17:19:33.78	-26:43:45.11	28.30	3.310	0.371	1.493	0.10	64.0
40		17:21:14.63	-26:53:01.38	23.15	3.286	0.380	1.848	0.05	174.1
41		17:22:27.64	-27:04:02.84	13.41	3.747	0.339	1.744	0.06	71.9
42		17:22:40.52	-27:05:04.19	9.83	3.797	0.306	3.193	0.07	150.4
43		17:21:58.97	-26:51:07.23	9.44	3.372	0.351	1.079	0.10	48.8
46		17:24:23.49	-26:32:03.82	35.38	3.090	0.334	0.407	0.05	37.9
47		17:27:26.27	-26:58:23.46	2.02	2.861	0.484	1.479	0.05	75.4
48		17:25:56.04	-26:44:23.72	2.21	3.611	0.326	2.983	0.06	83.0
51	a	17:27:22.81	-26:44:16.14	10.39	3.648	0.372	1.670	0.07	65.5
	b				3.030	0.601	0.563		
52	a	17:28:19.47	-26:44:02.04	1.77	3.577	0.334	0.853	0.04	50.8
	b				3.039	0.890	0.158		
54		17:30:24.12	-26:49:45.74	4.87	5.836	0.308	0.797	0.08	63.5
56		17:28:11.41	-26:24:09.44	8.46	3.613	0.502	1.547	0.05	85.7
57		17:31:03.73	-26:48:08.58	12.68	5.855	1.203	0.211	0.08	58.9
58	a	17:29:41.96	-26:29:16.61	11.15	3.774	0.772	0.298	0.05	50.8
	b				4.947	0.369	0.237		
59		17:30:49.24	-26:38:34.64	3.42	4.744	0.289	0.653	0.10	56.9
61		17:28:35.63	-26:16:47.08	31.72	3.826	0.448	0.575	0.07	67.7
63	2	17:31:34.85	-26:36:41.42	5.68	5.181	0.924	0.458	0.06	66.5
	a				5.444	0.379	0.504		
	b				4.923	0.457	0.442		
64		17:31:28.27	-26:31:41.48	3.07	5.086	0.491	1.411	0.06	80.1
65		17:31:20.68	-26:30:37.91	4.44	4.993	0.573	1.581	0.05	84.3
66		17:31:13.42	-26:29:02.25	12.90	4.909	0.627	1.377	0.05	82.1
67		17:28:41.88	-25:55:58.81	16.07	4.239	0.463	1.462	0.07	62.1
68		17:30:03.85	-26:03:00.02	20.95	4.458	0.398	0.589	0.11	52.4
70		17:29:37.99	-25:54:28.92	5.88	3.915	0.470	1.915	0.06	80.1
73		17:30:27.258	-25:59:28.57	1.39	4.264	0.361	0.531	0.05	56.4
74		17:32:36.32	-26:15:55.25	14.19	4.211	0.335	1.959	0.06	94.4
75		17:33:04.51	-26:11:24.06	27.99	5.140	0.485	0.648	0.07	62.2
79	2	17:33:08.57	-26:01:46.43	12.97	4.682	0.743	0.748	0.07	78.4
	a				4.843	0.481	0.688		
	b				4.421	0.372	0.553		
80		17:33:32.80	-26:01:42.21	13.72	4.693	0.453	1.075	0.07	81.2
81		17:28:36.50	-25:15:41.55	7.98	3.454	0.316	0.360	0.03	38.4
82		17:34:31.06	-26:02:46.66	32.11	6.356	0.500	0.315	0.05	58.4
84		17:34:51.62	-26:01:31.82	5.14	6.303	0.287	1.086	0.07	61.4
86		17:33:27.15	-25:43:44.12	26.04	4.437	0.403	1.446	0.14	86.5
87		17:34:30.38	-25:49:53.16	84.55	4.753	0.525	1.606	0.05	140.5
88		17:33:47.74	-25:43:36.70	39.54	5.470	0.491	0.979	0.12	91.6
89		17:33:28.54	-25:40:47.98	6.68	4.445	0.465	1.497	0.07	101.2
91		17:32:31.38	-25:25:16.92	20.35	4.195	0.376	1.134	0.05	85.2
92		17:34:04.99	-25:39:49.30	36.68	5.110	0.517	1.953	0.06	109.4
93	a	17:34:47.18	-25:46:29.21	34.42	5.221	0.554	1.530	0.15	126.5
	b				6.483	0.351	0.375		
94		17:34:35.50	-25:43:16.26	2.97	5.305	0.478	1.006	0.06	89.9
95		17:22:58.55	-23:58:03.80	5.53	4.763	0.501	0.541	0.03	38.5
96		17:23:34.99	-24:02:22.61	36.19	4.767	0.660	0.289	0.03	44.7
97	2	17:33:30.95	-25:30:31.25	20.77	4.128	1.000	0.870	0.04	109.8
	a				4.393	0.370	1.052		
	b				3.924	0.305	0.951		

TABLE 7
 C^{18}O DATA

	c				3.401	0.653	0.280		
98		17:34:40.17	-25:40:26.85	6.51	5.347	0.511	1.166	0.07	100.2
99		17:25:02.08	-24:12:57.98	20.10	4.714	0.296	1.466	0.10	56.0
100		17:32:44.405	-25:21:09.07	1.29	3.840	0.709	0.144	0.05	58.9
101		17:22:39.29	-23:49:59.01	12.99	3.342	0.276	1.648	0.12	81.7
102		17:34:20.53	-25:34:04.73	28.50	4.714	0.296	1.466	0.04	141.4
103		17:36:22.844	-25:49:51.72	1.31	2.830	0.313	1.236	0.05	51.8
105		17:25:10.82	-24:08:31.23	4.06	4.549	0.337	1.259	0.04	54.0
106		17:24:58.64	-24:06:50.64	14.12	4.773	0.313	0.973	0.04	54.9
108	2	17:31:31.51	-24:58:51.30	12.57	5.623	1.169	0.394	0.09	56.2
	a				5.863	0.359	0.634		
	b				5.244	0.331	0.487		
109		17:35:44.90	-25:33:02.00	17.87	5.846	0.380	2.420	0.05	132.8
110		17:28:38.67	-24:27:33.60	7.25	6.091	0.590	0.511	0.04	38.1
111		17:34:42.113	-25:20:28.85	1.32	3.595	0.679	0.295	0.04	62.7
112		17:23:48.45	-23:42:55.64	8.35	4.952	0.329	1.348	0.09	64.6
113		17:23:36.61	-23:41:03.62	16.45	4.675	0.368	1.161	0.09	67.3
114		17:23:05.58	-23:33:41.56	13.15	4.980	0.297	0.283	0.03	30.6
115		17:35:06.55	-25:20:57.07	8.18	3.999	0.400	0.625	0.13	70.4
118		17:35:40.31	-25:22:18.62	4.44	3.744	0.983	0.536	0.04	75.7
119		17:30:32.30	-24:35:27.55	4.09	5.245	0.511	0.470	0.10	51.0
120		17:27:17.43	-24:04:34.95	12.42	4.488	0.816	0.353	0.03	50.5
123	a	17:36:22.25	-25:23:04.26	26.51	3.771	0.316	1.282	0.08	77.9
	b				3.022	0.530	0.371		
127		17:36:30.85	-25:18:59.50	6.11	3.602	0.427	0.953	0.07	87.0
128		17:35:18.71	-25:07:55.03	10.19	15.079	1.043	0.338	0.08	58.0
130		17:37:07.28	-25:15:38.50	13.91	3.866	0.526	0.450	0.06	74.7
131		17:38:05.64	-25:17:06.13	8.16	3.511	0.466	1.168	0.09	81.3
132		17:37:50.86	-25:14:51.71	14.49	3.934	0.491	1.658	0.04	85.0
133		17:28:46.93	-23:53:46.54	10.67	3.156	0.418	1.881	0.11	56.0
135		17:38:58.21	-25:07:44.93	5.68	2.930	0.414	1.247	0.07	57.2
137		17:39:28.03	-25:07:13.19	0.69	2.478	0.325	0.975	0.20	52.7
140		17:39:41.74	-25:01:42.33	15.44	3.072	0.401	0.514	0.09	57.9
145		17:36:56.58	-24:19:29.52	27.72	3.155	0.252	0.433	0.04	50.1

(a) Flag given to indicate C^{18}O component for each extinction core. Components “a”, “b”, etc are ordered by antenna temperature. Where given, a Flag=2, corresponds to all components fit with a single Gaussian. (b) Total column density expressed in magnitudes of extinction (A_V) measured in a Gaussian weighted 56'' beam on the NICER 2MASS map of Lombardi et al. (2006) and centered on the position of the C^{18}O observation.